Postprint of: Jarzebowicz L., Karwowski K., Kulesza W. J., Sensorless algorithm for sustaining controllability of IPMSM drive in electric vehicle after resolver fault, Control Engineering Practice, Vol. 58 (2017), pp. 117-126, DOI: 10.1016/j.conengprac.2016.10.004


# Sensorless algorithm for sustaining controllability of IPMSM drive in electric vehicle after resolver fault

Leszek Jarzebowicz [1*], Krzysztof Karwowski [2], Wlodek J. Kulesza [3]

[1] Faculty of Electrical and Control Engineering, Gdansk University of Technology, Narutowicza st. 11/12, Gdansk, Poland; phone: +48 58 347 21 49, e-mail: leszek.jarzebowicz@pg.gda.pl (*corresponding author).

[2] Faculty of Electrical and Control Engineering, Gdansk University of Technology, Narutowicza st. 11/12, Gdansk, Poland; phone: +48 58 347 11 58, e-mail: krzysztof.karwowski@pg.gda.pl.

[3] Department of Applied Signal Processing, Blekinge Institute of Technology, SE-371 79 Karlskrona, Sweden; +46 45 538 58 98, e-mail: wlodek.kulesza@bth.se.

Highlights:

1. Special requirements for emergency-activated sensorless algorithms are defined
2. An emergency rotor position estimator based on motor currents derivatives is proposed
3. A low-resource algorithm implementation on digital signal processor is presented
4. Stable emergency activation is proven and estimation errors are quantified

Keywords: sensorless control, rotor position estimation, hybrid electric vehicles, flying-start, on-board diagnostics

Abstract: **This paper presents a sensorless algorithm designated for the emergency control of an interior permanent magnet synchronous motor (IPMSM) drive in electric or hybrid vehicle. Special requirements for emergency-activated sensorless algorithms are defined, and shortcomings of state-of-the-art methods in terms of the considered application are discussed. The proposed emergency-activated algorithm is based on analysing the derivatives of motor phase currents measured over the duration of particular inverter states. The method is computationally simple and does not require additional hardware since the derivatives are measured indirectly. A lag between activating the algorithm upon an emergency flying start and re-establishing the torque controllability is defined. The proposed algorithm was implemented in the controller of a laboratory IPMSM vehicle drive and tested under varying operational conditions, including the emergency activation.**

## 1. Introduction

Contemporary combustion cars are equipped with on-board diagnostics systems (OBDs) [1]. Such systems, introduced by U.S. legislative regulations in 1988, initially aimed to detect and indicate engine faults that could cause a significant increase in harmful emissions. Nowadays, OBDs detect almost all major malfunctions in the combustion car's drivetrain. In many cases, OBDs are able to isolate a faulty device and switch into a sub-optimal control mode, which uses the remaining sensors and actuators. It is expected that a similar development of drivetrain diagnostics will soon be implemented in electric vehicles (EVs) and hybrid-electric vehicles (HEVs). Currently, the U.S. Code of Federal Regulations states that a manufacturer has to equip a hybrid car with a monitoring system for the batteries [2]. It seems to be only a matter of time until legislative regulations will require diagnostics for the other drivetrain components of

EVs and HEVs, such as the electric motor, inverter and numerous sensors. Several methods of detecting and isolating the faults of such components have already been proposed [3][4][5][6][7][8].

If a fault occurs when driving, the faulty component must be immediately excluded from the drivetrain control. The control algorithm has to switch into the emergency mode in order to maintain vehicle controllability. This is particularly important for cars equipped with in-wheel electric drives where a fault of a single in-wheel drive may disrupt the balance of propulsive or breaking forces generated on individual wheels, which at high traveling speed can lead to the sudden deprivation of vehicle stability [9][10].

The majority of modern EVs and HEVs apply permanent magnet synchronous motor (PMSM) traction drives, usually of the interior type (IPMSM) [11][12]. Recently, an intensive research has been conducted on the sensorless control of IPMSM drives. In a case of sensorless control, the rotor-position feedback, required to control the motor's torque, is estimated instead using, for instance, a resolver. Such solution is applied to many industrial applications of these motors. However, the sensorless control has not yet been deployed onto the drives of mass-produced HEVs and EVs. Nevertheless, sensorless control algorithms could be used as a sub-optimal emergency procedure, activated upon the detection of rotor-position sensor failure [13][14].

The requirements for an emergency-activated sensorless control algorithm are found and studied in this paper. Two rotor-position estimators based on the derivatives of motor phase currents (DMPCs) are proposed. The estimator dedicated for medium and high speeds, previously presented in [15] as a sensorless-by-default solution, is now supplemented with a new low speed estimator. These two estimators are investigated in terms of their emergency activation ability. They are implemented and tested on a laboratory IPMSM drive, and the results confirm their fast emergency activation and stable operation in traction-specific operational conditions.

## 2. State of the Art

The sensorless control of vehicle drives is troublesome due to their wide range of operational speeds and the demand for uninterrupted torque controllability; therefore, a set of two estimation methods is typically used. At a low speed and standstill, the rotor's position is estimated from the analysis of stator inductances, which vary due to the rotor saliency. An additional high-frequency (HF) signal component, generated by the inverter, is required to measure the inductances [13][16][17]. At medium and high speeds, an estimation based on the electromotive force (EMF) observer is most convenient [18] [19].

The activation of the estimation algorithm during a drive operation, the so-called flying start, is considered in [13] and [14] where a typical combination of HF injection and EMF observer methods is

also used. Aguirre et al. [14] propose an additional procedure for the rough estimation of the rotor's position to pre-tune the target estimation algorithm.

Some unconventional approaches to the sensorless control of IPMSM drives have been proposed; however, they do not directly aim at vehicular applications. One of these approaches is based on DMPC analysis. DMPC methods are also referred to as: fundamental excitation [20][21], PWM transients [22], current ripples [23] and current-slope algorithms [24][25]. Recent research on DMPC methods is reviewed over the following paragraphs.

Hosogaya and Kubota propose an algorithm that enables the controller to estimate the rotor speed by analysing the DMPCs calculated for the $q$-axis [26]. They suggest that the rotor angle can be estimated as an integral of speed.

Research reported in [25] concerns an estimation algorithm that analyses current derivatives in order to calculate the rotor's position on the basis of IPMSM motor saliency. In turn, in [27] DMPCs are used to estimate the rotor's position from an electromotive force vector.

In [21], an estimator for a wide speed range is presented where the rotor's position is differently estimated in low- and high-speed ranges. Current derivatives are measured by means of Rogowski coils. Narrow inverter states are prolonged to measure the current derivative accurately.

An estimation algorithm for the rotor's position by analysing motor saliency is presented in [20]. The results show good estimation accuracy. However, the solution requires a major amendment to the PWM algorithm as well as hardware upgrades, such as a modification of IGBT gate circuits and an addition of current derivative sensors.

## 3. Problem Statement

The application of the emergency-activated rotor's position estimation algorithm involves special requirements compared with a drive that is sensorless-controlled by default. Such an algorithm:

a) has to provide a reliable feedback instantly, even if it becomes activated with an unknown initial position and speed.

b) should not require any hardware upgrades compared with the resolver-based control in order not to increase cost and complexity. This mainly concerns current feedback components, such as transducers and analogue-to-digital converters (ADCs).

c) should be simple and quickly computed to fit into the time window within a control cycle, which is reserved for emergency algorithms. Since the target drive is expected to consist of numerous emergency algorithms for various malfunctions, these algorithms have to be started on the occurrence of particular faults, leaving the reserved time window idle during normal operation.

As faults are expected to be uncommon and the aim of the emergency algorithm is to sustain vehicle's stability and controllability, sub-optimal solutions are accepted. Therefore, the estimates of the rotor's position are not expected to be as accurate as in typical sensorless drives. Further, a slight decrease in drive performance is admissible. However, the emergency estimation algorithm should be robust to all traction-specific operational conditions in order to assure vehicle's controllability and stability.

As one can see from the review of related papers, only a typical approach of combining the HF injection and EMF observer methods has been considered as a solution to the resolver-fault emergency control of traction drives. The HF injection methods require additional controller resources and hardware filters, which does not comply with the requirement (b). In turn, the inceptive performance of observers is highly affected by the initial values of state variables; therefore, their flying start must be preceded by an initialisation procedure, which does not follow the requirement (a). This problem may be overcome by running the observer constantly in the background; however, this would collide with the requirement (c).

A DMPC-based method can overcome the aforementioned drawbacks. A use of the current derivatives in the motor's mathematical model makes it possible to apply simple estimation equations, which do not consist of integrals; therefore, state-variables initialisation constraints are omitted and the processing time is reduced. At the same time, the estimator does not load the controller until a resolver fault occurs, which maintains the computing overhead for other emergency algorithms. Current derivatives may be measured indirectly by sampling the currents more frequently than a typical control method requires, which discards the requirement of installing *di*/*dt* sensors.

In this paper, we propose the DMPC-based algorithm designated for the emergency-mode sensorless control of traction IPMSM drive. The DMPC-based methods are sensitive to measurement disturbances, thus the reported solutions often consist of an advanced current-measuring hardware as well as a sophisticated signal processing in order to provide the rotor's position accurate estimates. Following the special requirements of our application, we propose the method featured by simple computations and lacking hardware amendments. In turn, this method is not expected to be as accurate as the sensorless-by-default solutions, as long as the control stability and fast flying start are ensured.

## 4. Sensorless Control Algorithms

The general structure of the control algorithm is shown in Fig. 1. The algorithm is based on the fundamental torque control and voltage modulation methods, which are presented in the following subsection. The controller applies standard motor phase current measures to compute DMPCs, as explained in Subsection 4.2. The motor mathematical model, presented in Subsection 4.3, is fundamental

for the rotor-position estimators introduced in Subsections 4.4 and 4.5. As the algorithms aim to estimate the position of the rotor, the angular speed is computed by differentiation.

### 4.1. Torque Control and Voltage Modulation Methods

A fundamental diagram of the field-oriented control (FOC) algorithm is included in Fig. 1. Motor currents are regulated in the *d-q* reference frame, rotating synchronously with the rotor speed. A reference torque is set according to the maximum torque per ampere (MTPA) strategy or flux weakening (FW), following the actual angular speed $\omega$.

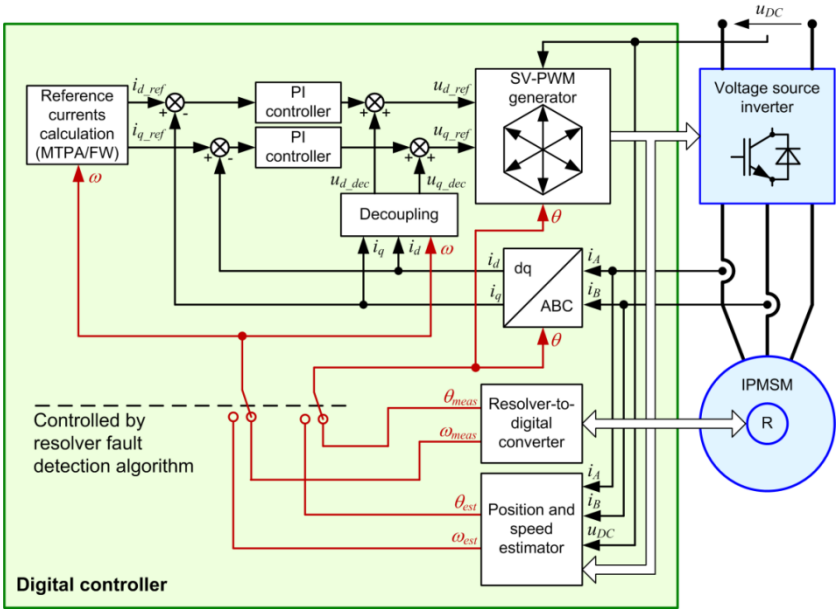


**Fig. 1.** General structure of the drive-control algorithm consisting of an emergency rotor-position estimator

Generation of the inverter's output voltage, respective to the reference value, is based on the space vector pulse width modulation (SV-PWM) method, that is, by a sequence of inverter states. An inverter's electrical diagram and the output voltage vectors resulting from possible inverter states are presented in Fig. 2a and Fig. 2b, respectively. Usually, the modulation cycle consists of four active and three passive states, which are located symmetrically with respect to the mid-point of the PWM cycle, as shown in Fig. 2c. The active vectors $\underline{v}_m$ and $\underline{v}_n$ are selected as an adjacent pair from the set of $\underline{v}_1 - \underline{v}_6$ (see Fig. 2b).

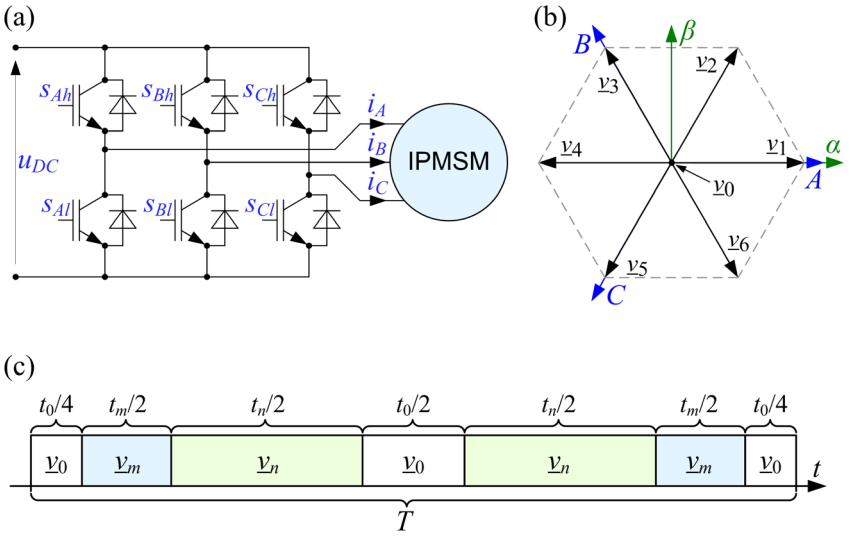


**Fig. 2.** Voltage source inverter: (a) Electrical diagram; (b) Inverter's output voltage vectors $\underline{v}_1$ – $\underline{v}_6$ in $\alpha$-$\beta$ and $ABC$ reference frames; (c) Timing of inverter's states during an SV-PWM cycle

### 4.2. Indirect Measurement of DMPCs

The basis of the indirect DMPC measurement approach is shown in Fig. 3. During a stable inverter state, the voltages at the motor terminals are constant. Motor currents vary exponentially, but the state duration is relatively short compared with the electrical time constant. Therefore, it can be linearly approximated so that a current derivative can be calculated as a difference quotient $\Delta i/\Delta t$.

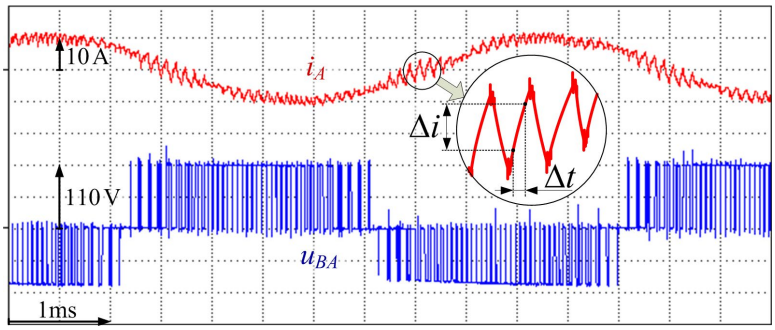


**Fig. 3.** Waveforms of phase current $i_A$ and line-to-line voltage $u_{BA}$ in an IPMSM motor supplied by the voltage source inverter (VSI) [15]

### 4.3. IPMSM Model

The following equations are essential for the estimators presented in the next subsections:

$$\frac{di_d}{dt} = \frac{1}{L_d}\left(-R_s i_d + L_q p\omega_m i_q + u_d\right), \tag{1}$$

$$\frac{di_q}{dt} = \frac{1}{L_q}\left(-R_s i_q - L_d p\omega_m i_d - p\omega_m \psi_f + u_q\right), \tag{2}$$

where: $i_d$, $i_q$, $u_d$, $u_q$, $L_d$ and $L_q$ are: the $d$- and $q$- axis components of the stator's current, voltage and inductance, respectively; $\psi_f$ is the flux linkage due to the rotor magnets; $R_s$ is the stator's resistance; $\omega_m = \omega/p$ is the mechanical speed; and $p$ is the number of pole pairs.

In order to estimate rotor's position with respect to a stationary reference frame, Clarke and Park transformations are used; see Fig. 2b for the axes labelling the stationary frames $ABC$ and $\alpha$-$\beta$.

The derivatives, $di_d/dt$ and $di_q/dt$, are affected by many inputs, of which an EMF $p\omega_m\psi_f$ and the stator's inductances $L_d$, $L_q$ can be used to compute the rotor's angular position. The computation of the angle of the EMF vector is convenient for estimating the rotor's position at medium and high speeds. At low speed, when the EMF is also low, its influence on DMPCs is hard to detect due to a measurement noise. In this case, an analysis of the stator's inductances can be used to estimate the rotor's position.

### 4.4. Proposed EMF-Based Estimator

The rotor-position estimation algorithm, initially proposed for sensorless-by-default drives in [15], uses DMPCs measured for the passive inverter state $\underline{v}_0$ to compute the DMPC vector, whose argument $\gamma$ is influenced mainly by the EMF. The argument of the DMPC vector is used as a reference angle to estimate the rotor's position. The angular position of the DMPC vector can be related both to the $\alpha$-axis of the stationary reference frame:

$$\gamma_{\alpha-\beta} = \arg\left(\frac{d\underline{i}_{(v0)}}{dt}\right)_{\alpha-\beta} \tag{3}$$

and to the $d$-axis of the $d$-$q$ rotating reference frame:

$$\gamma_{d-q} = \arg\left(\frac{d\underline{i}_{(v0)}}{dt}\right)_{d-q}. \tag{4}$$

Thus, the rotor's angular position $\theta$ can be computed by subtracting $\gamma_{d\text{-}q}$ from $\gamma_{\alpha\text{-}\beta}$, as shown in Fig. 4a, where the angle $\gamma_{\alpha\text{-}\beta}$ is obtained by measuring the DMPCs:

$$\gamma_{\alpha-\beta} = \arctan\left(\frac{di_{\beta(v0)}}{dt} \Big/ \frac{di_{\alpha(v0)}}{dt}\right). \tag{5}$$

In turn, to derive the value of $\gamma_{d\text{-}q}$, the motor's model equations are used, as explained further in this section.

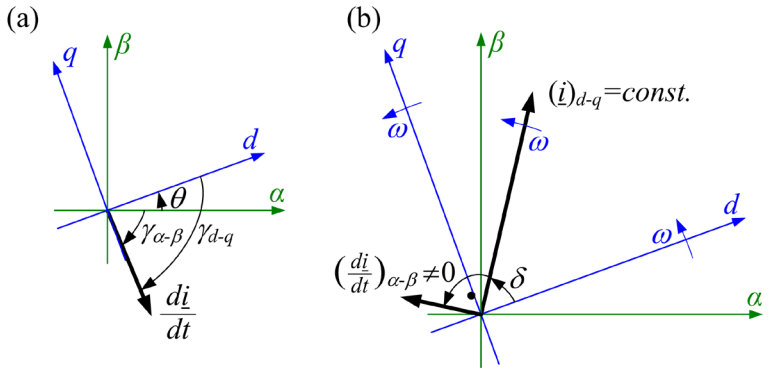


**Fig. 4.** DMPC vectors in different reference frames: (a) Position of the DMPC vector with respect to the $\alpha$-$\beta$ and $d$-$q$ frames; (b) DMPC movement-related vector component $(d\underline{i}/dt)_{\alpha\text{-}\beta}$ observed in the $\alpha$-$\beta$ frame due to the rotor's movement

The rotor-position estimator is designated for an operation at medium and high speeds; therefore, the voltage drop on stator's resistances can be neglected. Moreover, motor's voltages $u_d$ and $u_q$ equal zero if the passive inverter state is considered. Consequently, (1) and (2) are simplified as follows:

$$\frac{di_{d(v0)}}{dt} = \frac{L_q}{L_d} p\omega_m i_q = \omega \frac{L_q}{L_d} i_q, \tag{6}$$

$$\frac{di_{q(v0)}}{dt} = -\frac{L_d}{L_q} p\omega_m i_d - \frac{1}{L_q} p\omega_m \psi_f. \tag{7}$$

Considering the typical motor's parameters and medium- or high-speed operation, the EMF term $p\omega_m\psi_f/L_q$ is distinctly dominant; therefore, the DMPC vector's position can be roughly approximated as $\gamma_{d\text{-}q} \cong -\pi/2$. However, to minimise the estimation error of the rotor's position, the angle $\gamma_{d\text{-}q}$ should be computed based on the motor-model parameters and instantaneous $d$-$q$ current components included in (6) and (7):

$$\gamma_{d-q} = \arctan\left(\frac{di_{q(v0)}}{dt} \Big/ \frac{di_{d(v0)}}{dt}\right). \tag{8}$$

To compute the rotor's angular position $\theta$, it is required to include DMPCs in both the *ABC* and $\alpha$-$\beta$ reference frames. It is convenient to apply the Park transformation for this purpose; however, when the transformation is applied to derivatives, it causes a systematic error due to the rotor movement. This error can be determined by extracting a component of the DMPC vector that corresponds to the rotor movement. In order to do that, a theoretical case is studied where the derivative is computed for a current vector $\underline{i}$ having the constant modulus $|\underline{i}|$ and angle $\delta$ in the $d$-$q$ reference frame, as shown in Fig. 4b. The derivative of this vector $(d\underline{i}/dt)_{d\text{-}q}$, observed in the $d$-$q$ reference frame, equals zero. However, the derivative $(d\underline{i}/dt)_{\alpha\text{-}\beta}$, computed for the $\alpha$-$\beta$ frame, does not equal zero, since it reflects the movement of the $d$-$q$ frame. This movement-related component $(d\underline{i}/dt)_{\alpha\text{-}\beta} = d\underline{i}_\omega/dt$ can be decomposed into $d$ and $q$ components for later inclusion into the estimator equations:

$$\frac{di_{d\omega}}{dt} = -\omega \cdot |\underline{i}| \cdot \sin\delta = -\omega \cdot i_q \,, \tag{9}$$

$$\frac{di_{q\omega}}{dt} = \omega \cdot |\underline{i}| \cdot \cos\delta = \omega \cdot i_d \,. \tag{10}$$

Consequently, the angle $\gamma_{d\text{-}q}$ given by (8) needs to be corrected by:

$$\gamma_{corr} = \arctan\left(\frac{di_{q\omega}}{dt} \Big/ \frac{di_{d\omega}}{dt}\right). \tag{11}$$

Finally, the rotor-position estimation formula is given as:

$$\theta = \gamma_{\alpha-\beta} - \gamma_{d-q} - \gamma_{corr} \,. \tag{12}$$

As discussed in [15], the term $-\gamma_{d\text{-}q}-\gamma_{corr}$ is related to the current $i_q$ both in the MTPA and in the FW current-control strategies. This relation for the motor parameters, given in Table 1, is presented in Fig. 5. The drive's overload capacity can be used below the base speed; therefore, in the case of using the MTPA strategy, the current $i_q$ reaches a value of twice that of the rated current. As one can see, the term $-\gamma_{d\text{-}q}-\gamma_{corr}$ can be well approximated by a linear function of $i_q$ for both considered control strategies. Then, the simplified formula for the rotor-position estimation is given by:

$$\theta \cong \gamma_{\alpha-\beta} + \frac{\pi}{2} - k \cdot i_q = \arctan\left(\frac{di_{\beta(v0)}}{dt} \Big/ \frac{di_{\alpha(v0)}}{dt}\right) + \frac{\pi}{2} - k \cdot i_q = \arctan\left(\frac{di_{\alpha(v0)}}{dt} \Big/ -\frac{di_{\beta(v0)}}{dt}\right) - k \cdot i_q \,, \tag{13}$$

where the constant $k$ is computed based on the motor parameters.

The rotor's position is estimated using the current $i_q$, which has to be computed knowing the rotor's position. In practice, it means that the value of $i_q$ must be taken from the previous control cycle. As shown in Fig. 5, when the current $i_q$ varies from zero to twice that of the rated value, the term $-\gamma_{d\text{-}q}-\gamma_{corr}$ changes by approximately $0.03\pi$ rad (less than 15°). Therefore, one can notice the method's low sensitivity to motor parameters and to the current $i_q$, which is computed based on the estimated rotor's position in the preceding computation cycle.

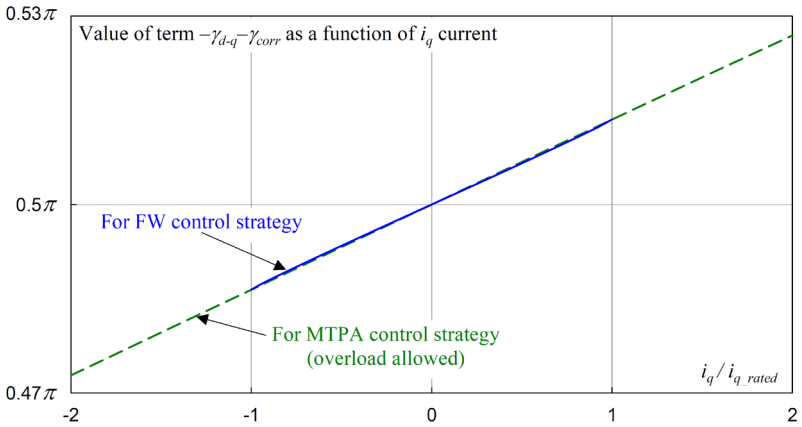


**Fig. 5.** Relationship of $-\gamma_{d\text{-}q}-\gamma_{corr}$ vs. $i_q$ for the motor's model parameters given in Table 1 [15]

### 4.5. Proposed Saliency-Based Estimator

The proposed low-speed estimator computes the rotor's position on the basis of the stator's inductances. In IPMSM motors, permanent magnets are placed inside the rotor, which leads to that the *d*-axis inductance to be significantly smaller than the *q*-axis inductance. This feature, called saliency, causes the stator inductance to be a function of the double rotor's angular position. The proposed algorithm applies an approach similar to the one presented in [28]; however, its computations are simplified.

The inductance variation can be investigated by applying the voltage vector at a certain angle and measuring the induced current derivatives. However, the derivatives are also influenced by EMF, if the rotor is moving. Nevertheless, this effect can be diminished by performing an additional *di/dt* measurement for the zero-voltage state. As long as both *di/dt* measurements are performed within a short time, motor's currents $i_d$ and $i_q$, rotor's speed $p\omega_m$ and rotor's position $\theta$ may be assumed constant. Then, the derivatives obtained by applying voltage vectors to the distinctive *d* and *q* axes are given by:

$$\frac{di_{d(ud)}}{dt} - \frac{di_{d(v0)}}{dt} = \frac{1}{L_d}\left(-R_s i_d + L_q p\omega_m i_q + u_d\right) - \frac{1}{L_d}\left(-R_s i_d + L_q p\omega_m i_q\right) = \frac{u_d}{L_d}, \tag{14}$$

$$\frac{di_{q(uq)}}{dt} - \frac{di_{q(v0)}}{dt} = \frac{1}{L_q}\left(-R_s i_q - L_d p\omega_m i_d - p\omega_m \psi_f + u_q\right) - \frac{1}{L_q}\left(-R_s i_q - L_d p\omega_m i_d - p\omega_m \psi_f + u_q\right) = \frac{u_q}{L_q}. \tag{15}$$

where: $\underline{u}_d = u_d e^{j\theta}$ and $\underline{u}_q = u_q e^{j(\theta+\pi/2)}$ are the voltage vectors aligned to the *d*- and *q*-axes, respectively.

Consequently, the rotor's position can be estimated by applying the voltage vectors of constant moduli and varying arguments and determining the *d*-axis direction as the argument of the vector that induces the highest *di/dt* response. Nevertheless, since the voltage source inverter can apply only six active voltage vectors $\underline{v}_1$– $\underline{v}_6$, defined in Fig. 2b, whose arguments are spaced by $\pi/3$, then, a specific method is required to improve the angular resolution of determining the direction with the highest *di/dt*.

The proposed approach is based on applying the vectors $\underline{v}_1$, $\underline{v}_3$, $\underline{v}_5$, and $\underline{v}_0$. To obtain the *di/dt* response exclusively for the active voltage vectors, the influence of EMF is excluded by subtracting the derivatives corresponding to the zero-voltage state:

$$\frac{di_A}{dt} = \frac{di_{A(v1)}}{dt} - \frac{di_{A(v0)}}{dt}, \tag{16}$$

$$\frac{di_B}{dt} = \frac{di_{B(v3)}}{dt} - \frac{di_{B(v0)}}{dt}, \tag{17}$$

$$\frac{di_C}{dt} = \frac{di_{C(v5)}}{dt} - \frac{di_{C(v0)}}{dt}. \tag{18}$$

The derivatives (16)–(18), calculated for each motor phase, are used to compute a vector whose argument matches the *d*-axis position:

$$2\theta = \arg\left( \frac{di_A}{dt} e^{j0} + \frac{di_B}{dt} e^{j\left(\frac{2\pi}{3}\right)} + \frac{di_C}{dt} e^{j\left(\frac{4\pi}{3}\right)} \right). \quad (19)$$

As the algorithm tracks the *d*-axis by seeking the direction corresponding to the minimal stator's inductance, it is robust to variation in the motor parameters as long as the *d*-axis inductance is distinctively lower than the *q*-axis inductance.

## 5. Algorithm Implementation

### 5.1. Experimental Test Stand

The proposed estimation algorithm was implemented in a laboratory IPMSM drive that uses a typical industrial-class controller. The drive has a structure similar to that presented in Fig. 2. The identified parameters of the motor are given in Table 1.

**Table 1.** IPMSM parameters used in the experimental setup

| Parameter | Value |
|---|---|
| Stator's resistance $R_s$ | 0.12 Ω |
| *d*-axis component of stator's inductance $L_d$ | 0.90 mH |
| *q*-axis component of stator's inductance $L_q$ | 1.05 mH |
| Flux linkage due to the rotor's magnets $\psi_f$ | 75 mWb |
| Number of pole pairs $p$ | 9 |
| Rated DC-bus voltage $U_{DC}$ | 216 V |
| Rated motor's current $I_r$ | 10 A |
| Rated motor's speed $\omega_r$ | 1300 rad/s |

The digital controller, based on the TMS320F2812 digital signal processor (DSP), performs the FOC algorithm. The control variables are transmitted from the DSP to a PC via the serial interface port. The standard SV-PWM voltage modulation method is used at a frequency of 10 kHz. Current transducers of the LTS-15NP type, with 0–100 kHz bandwidth, are chosen to measure the motor phase currents.

### 5.2. Configuration of DSP Peripherals

***Synchronised Current Sampling:*** The ADC module integrated into the DSP is set to perform a multiple sampling of $i_A$ and $i_B$ currents over a PWM cycle in order to measure DMPC indirectly. The instants of current sampling are related to the edges in the transistors' control signals. The sampling is triggered by a comparator, which incorporates the same counter as that used to generate the PWM signals. Thus, to sample synchronously with PWM signals' edges, it is exclusively required to copy the content of the

compare registers from the PWM peripheral block into the ADC module. In turn, the sampling instant with respect to the PWM signal can by simply shifted by adding a constant to the value of an ADC compare register.

The sampling is controlled by a conversion sequence manager and does not interfere with the main program execution. The reconfiguration of the ADC module is performed by setting designated registers and takes effect in the next PWM cycle. The detailed description of the ADC module setup is provided in [29].

***DMPC Computation for EMF-Based Estimation:*** The EMC-based estimator uses DMPCs measured during passive inverter states $\underline{v}_0$. In general, there are passive states in every PWM cycle. However, in the case of a high reference voltage, the duration of the passive states may be too short to allow a precise DMPC measurement. Therefore, the maximum reference voltage has to be limited to ensure a sufficient duration of the inverter's passive states.

DMPC computation is performed by using the accumulated current change approach, as presented in [29]. A timing example of the current sampling is shown in Fig. 6a. An SV-PWM cycle includes three passive states $\underline{v}_0$, marked at the bottom of the figure. The last passive state in the $k$-1 modulation cycle and the first passive state in the $k$ cycle are merged. Hence, only four current samples are necessary to calculate the accumulated current change $\Delta i_\Sigma$ of all passive states:

$$\Delta i_{\Sigma(k)} = \left(i_{t2(k)} - i_{t1(k)}\right) + \left(i_{t4(k)} - i_{t3(k-1)}\right), \tag{20}$$

where: $i_{t1}$– $i_{t4}$ are the successive current measurements (Fig. 6a) and $k$ is the number of PWM cycles.

The accumulated current change $\Delta i_\Sigma$ is computed exclusively for the $i_A$ and $i_B$ currents and transformed into an $\alpha$-$\beta$ reference frame to estimate the rotor's position in accordance with (13). Since the accumulated current changes are derived for the same time duration, the estimation formula (13) is simplified, thus:

$$\theta_{(k)} = \arctan\left(\Delta i_{\Sigma\alpha(k)} / -\Delta i_{\Sigma\beta_{(k)}}\right) - k \cdot i_{q(k-1)}. \tag{21}$$

The estimated rotor's position is updated in each PWM period. The first estimate, in the case of the switching from saliency-based estimation or in the case of the flying start, is obtained after three PWM periods: one for the DSP peripherals configuration, and two for measurements and computation.

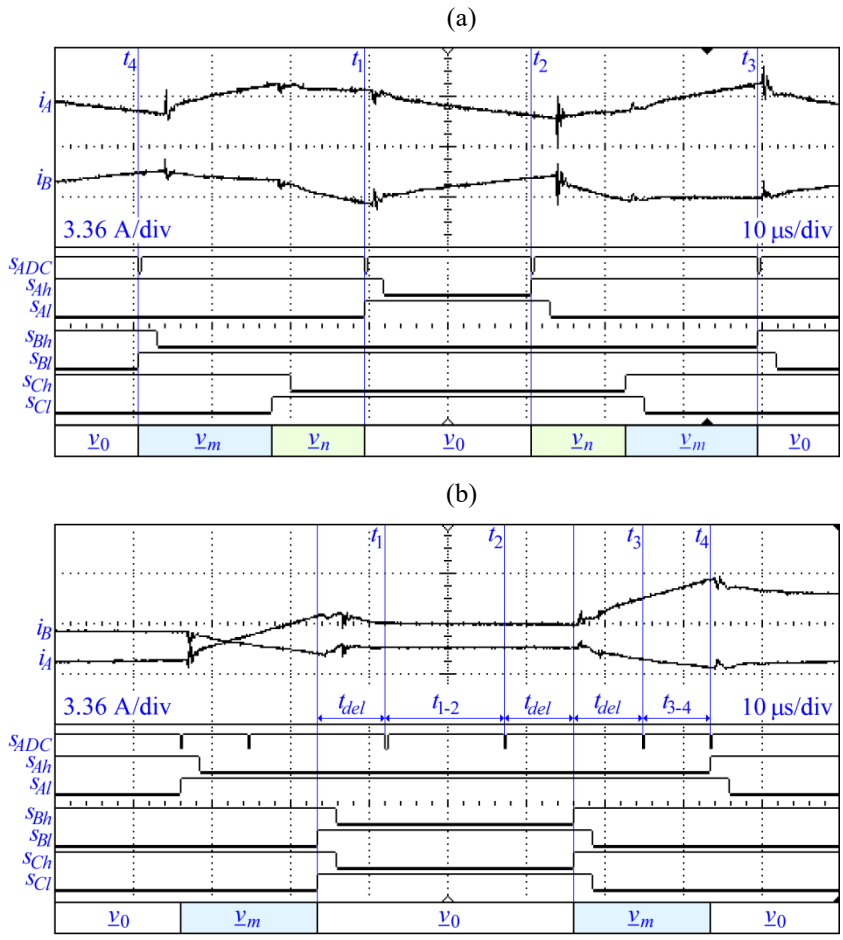


**Fig. 6.** Waveforms of the phase currents and control signals recorded in the IPMSM drive, where: $i_A$ and $i_B$ are motor's phase currents, $s_{ADC}$ is the ADC's conversion start signal (falling edge) and $s_{Ah} - s_{Cl}$ are the transistor control signals labelled as in Fig. 2a: (a) during the EMF-based estimator operation [29]; (b) during the saliency-based estimator operation

***DMPC Computation for Saliency-Based Estimation:*** The saliency-based estimator requires DMPCs measured for the following inverter states: $\underline{v}_1$, $\underline{v}_3$, $\underline{v}_5$ and $\underline{v}_0$. A use of the combined FOC and SV-PWM algorithms does not provide a set of these vectors during a single or several successive inverter states. Therefore, some additional means are required in order to allow for cyclic DMPC measurement and rotor's position estimation. The proposed solution uses test vectors, which are applied once in each of four PWM cycles, as shown in Fig. 7. The three test vectors, $\underline{u}_{TA} = u_T e^{j0}$, $\underline{u}_{TB} = u_T e^{j2\pi/3}$ and $\underline{u}_{TC} = u_T e^{j4\pi/3}$, are applied alternately, where $u_T$ must be adjusted to trade-off between estimation accuracy and current ripples. The PWM sequences corresponding to the test vectors consist of the passive state $\underline{v}_0$ and one of the active states: $\underline{v}_1$, $\underline{v}_3$ and $\underline{v}_5$. The introduction of the test vectors pauses the control algorithm and causes significant torque ripples; however, it does not interfere with the SV-PWM algorithm, which is typically hardware-implemented in DSPs. Therefore, it is easy to implement on a flying start.

The sampling timing for a selected test vector is presented in Fig. 6b. The DMPCs resulting from the active inverter states are computed as a difference quotient of the samples acquired at instants $t_3$ and $t_4$. The derivative for the passive inverter state is computed in the same manner, using samples acquired at instants $t_1$ and $t_2$. Instants $t_1$ and $t_3$ are delayed by $t_{del}$ with respect to the transistor control signals, so that the switching disturbances fade out and do not affect the measurement. Consequently, the $di/dt$ responses to the active voltage vectors are given as:

$$\frac{di_A}{dt} = \frac{di_{A(v1)}(t_4) - di_{A(v1)}(t_3)}{t_{3-4}} - \frac{di_{A(v0)}(t_2) - di_{A(v0)}(t_1)}{t_{1-2}}, \tag{22}$$

$$\frac{di_B}{dt} = \frac{di_{B(v1)}(t_4) - di_{B(v1)}(t_3)}{t_{3-4}} - \frac{di_{B(v0)}(t_2) - di_{B(v0)}(t_1)}{t_{1-2}}, \tag{23}$$

$$\frac{di_C}{dt} = \frac{di_{C(v1)}(t_4) - di_{C(v1)}(t_3)}{t_{3-4}} - \frac{di_{C(v0)}(t_2) - di_{C(v0)}(t_1)}{t_{1-2}}. \tag{24}$$

Since the intervals $t_{1\text{-}2}$ and $t_{3\text{-}4}$ refer to inverter's states which are performed immediately one after another (see Fig. 6b), the assumption stated in Section 4.5, that the currents and rotor's position and speed can be treated as constant, is fulfilled.

The derivatives (22)–(24) are used to compute the argument of vector $\underline{d}$ according to (19). The estimated rotor's position is updated once every fourth PWM cycle. The first value, in the case of switching from the EMF-based estimation or upon the emergency activation, is obtained after ten PWM periods: one configuration period of the DSP peripherals plus nine measurement and computation periods.

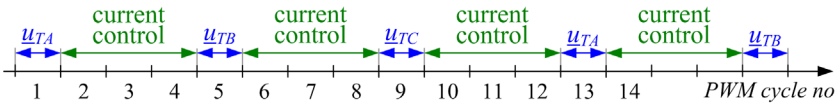


**Fig. 7.** Timing of interruption cycle of the FOC algorithm by overwriting the reference voltage in order to enable the saliency-based estimator to perform the necessary measurements

### 5.3. Parameter Setup

Some parameters, as mentioned in the implementation description, have to be adjusted to compromise between the various criteria of drive performance; however, this problem is beyond the scope of the paper. The settings of the experimental tests are discussed briefly in this section.

The reference voltage, when applying the EMF-based estimator, is limited to $k_U = 90\%$ of its maximum value. This ensures that each PWM cycle duration comprises at least 10% of passive states. The lower $k_U$ improves the estimates, as it results in higher current changes $\Delta i$, decreasing the effect of

disturbances and of the limited ADC resolution on the accuracy of DMPC measurement. But then, reducing $k_U$ decreases the ratio of voltage utilisation and therefore diminishes the drive's maximal power.

The moduli of the test vectors, which are used by the saliency-based method, are set to $u_T = 50$ V. The resulting total duration of the active states is 30% of the PWM cycle. Increasing $u_T$ leads to better estimation accuracy; however, it causes bigger current ripples. The $t_{del}$ time, shown in Fig. 6b, is set to 8.8 µs.

The threshold value of the rotor speed, at which the estimation methods switch, is set to $\omega_{tr} = 70$ rad/s. At this speed, the estimation errors for both the saliency and EMF-based estimators are similar. Upon the transition between these estimation methods, the control algorithm holds the last value provided by the switched-off method until the switched-on method delivers the first estimate. A similar scenario is applied on the emergency start-up of the sensorless control. By considering the activation time and operational speed of the algorithms, the rotor's displacement during the position holding does not exceed 0.4 rad (23°) for the EMF-based estimator and 0.1 rad (6°) for the saliency-based method.

As both estimators use only instant DMPCs, they are relatively sensitive to the measurement inaccuracy. The stochastic component of the rotor-position estimate is reduced by averaging the estimates of the past 16 PWM cycles. The outcome of averaging is corrected by a linear function of rotor's speed to compensate the computing delay.

## 6. Experimental Validation

Vehicular applications of electric drives are very demanding in terms of the range of operational conditions such as a speed, load and reference torque, and driving mode. Therefore, the sensorless control methods have to be verified in severe experimental tests consisting of compound operating scenarios. The main aim of our experimental tests is to prove that the control algorithm can be instantly switched into the sensorless mode upon an occurrence of a resolver fault and that this sensorless mode enables the drive to operate stably in all crucial, traction-specific conditions. Moreover, the test should help assess the general accuracy of the position estimation.

Three test scenarios are implemented to validate the proposed methods. The first scenario aims to verify the system's ability to operate at near-zero speed with the full torque reference when the drive control algorithm operates in the sensorless mode. The resolver is used exclusively to evaluate the error of the rotor's position estimation. The motor is loaded by a friction brake, modelling the inertial and resistance force of a vehicle. The test includes the multiple $i_q$ current step transitions between 0 A and the rated value of 10 A, as shown in the first graph in Fig. 8a. The drive starts from the standstill using the

saliency-based estimator. At the negative $i_q$, applied in 0.5-1 s, the drive accelerates up to 50 rad/s in a reverse direction. Then, the drive is set to freewheeling mode (1-1.5 s, $i_q = 0$), where it is stopped by the load torque. Afterwards, the negative $i_q$ interval is returned (1.5-2 s), but in the final stage, it changes to positive $i_q$, which causes a rapid regenerative braking and acceleration in a forward direction. During the saliency-based estimator operation, a substantial ripple component appears on the $i_q$ current waveform due to applying the test vectors. The fundamental frequency of this ripple component is approx. 1 kHz. This causes an unpleasant acoustic noise but does not result in perceptible vibrations. After the drive accelerates to the threshold speed of 70 rad/s, the estimation algorithm switches to the EMF-based method, which does not effect in any current ripples. During the test, the drive operates stably, and the estimation error depends on the magnitude and the dynamics of $i_q$; however, still the error does not exceed 0.7 rad (40°), as seen from the results shown in Fig. 8a.

The second test scenario (Fig. 8b) combines the wide-speed operation and switching between driving modes. The current $i_q$ changes among positive, zero and negative values, which correspond to propelling, freewheeling and breaking, respectively. No additional load torque is applied; therefore, the drive reaches the threshold speed of 70 rad/s quickly then applies the EMF-based estimator most of the time. At instant $t \cong 5$ s, the control strategy switches from MTPA to FW. Afterwards, an inverter's output current reaches its limit, which forces the reduction of the current $i_q$ in order to sustain the FW capability (i.e. a proper level of the current $i_d$). These operating conditions correspond to the shortest zero-voltage inverter states used by the EMF-based estimation algorithm. The results of the second validation scenario, shown in Fig. 8b, prove that the drive operates stably. The maximal error for the saliency-based estimation is the same as that of the first test scenario. The EMF-based method shows more accurate performance of a maximal position error of 0.4 rad (23°) for the medium-speed operation. At speeds exceeding 300 rad/s, the maximal position error is around 0.1 rad (6°). The EMF-based estimator is robust to both the magnitude and the dynamics of $i_q$. It also shows robustness to motor's speed for a range from 25% to 100% of rated speed.

The applied two test scenarios verified the proposed estimators and prove their stability in the vehicle-specific operating conditions. The assessment summary of the estimation accuracy is given in Table 2.

**Table 2.** Evaluation of the rotor's position estimation accuracy

| Estimation mode and operating conditions | Peak error | RMS error |
|---|---|---|
| Scenario 1 (time range: 0 s – 2.8 s) | 0.7 rad | 0.19 rad |
| Saliency-based estimation | (40°) | (11°) |
| Scenario 2 (time range: 0 s –0.55 s) | 0.7 rad | 0.22 rad |
| Saliency-based estimation | (40°) | (13°) |
| Scenario 2 (time range: 0.55 s – 1.65 s) | 0.4 rad | 0.11 rad |
| EMF-based estimation at speeds 70–300 rad/s | (23°) | (6°) |
| Scenario 2 (time range: 1.65 s – 7 s) | 0.1 rad | 0.04 rad |
| EMF-based estimation at speeds above 300 rad/s | (6°) | (2°) |

The third scenario concerns the drive's behaviour upon the resolver malfunction. The laboratory drive consists of the RDC integrated in AD2S1200 by Analog Devices, which provides a loss-of-signal indicator for the controller. This indicator turns to a high state upon the resolver's failure detection. The controller reads this indicator's status in each control cycle, and upon the failure detection switches into the emergency sensorless control mode. During the tests, the resolver's malfunction was affected by disconnecting resolver's sine and cosine circuits from the RDC during drive operation.

The emergency activation of the sensorless control has been successfully performed for various speeds and torques. The exemplary test results, for the activation at a half of the rated speed and a half of the rated torque, are presented in Fig. 8c. For this case, one can see data from the controller's digital outputs programmed to indicate execution times of the ADC setup procedure (waveform 3) and of the EMF-based estimator (waveform 4). Furthermore, data from the RDC loss-of-signal indicator (waveform 2) and the mechanical torque derived from a torque-meter fixed to the motor's shaft (waveform 1) are shown. In addition to that, the controller's variables related to rotor's position were memorized. Accordingly to the loss-of-signal indicator, the resolver's fault happened within the third recorded control cycle. After the fault indication, the controller initiated the sensorless mode by setting up the ADC for the multiple current sampling. Under the fourth and fifth cycles, the current samples were collected to compute the first DMPCs included in (21). During these cycles, the torque control algorithm used the last data of rotor's position received from the RDC before the malfunction was indicated. Starting from the sixth cycle, the drive was operated in the sensorless mode using the EMF-based estimator, where the rotor's position was computed in each control cycle and computation results were provided to the control algorithm. As seen in the topmost waveform in Fig. 8c, the emergency activation ran smoothly and did not cause any perturbation in the torque.

(a)

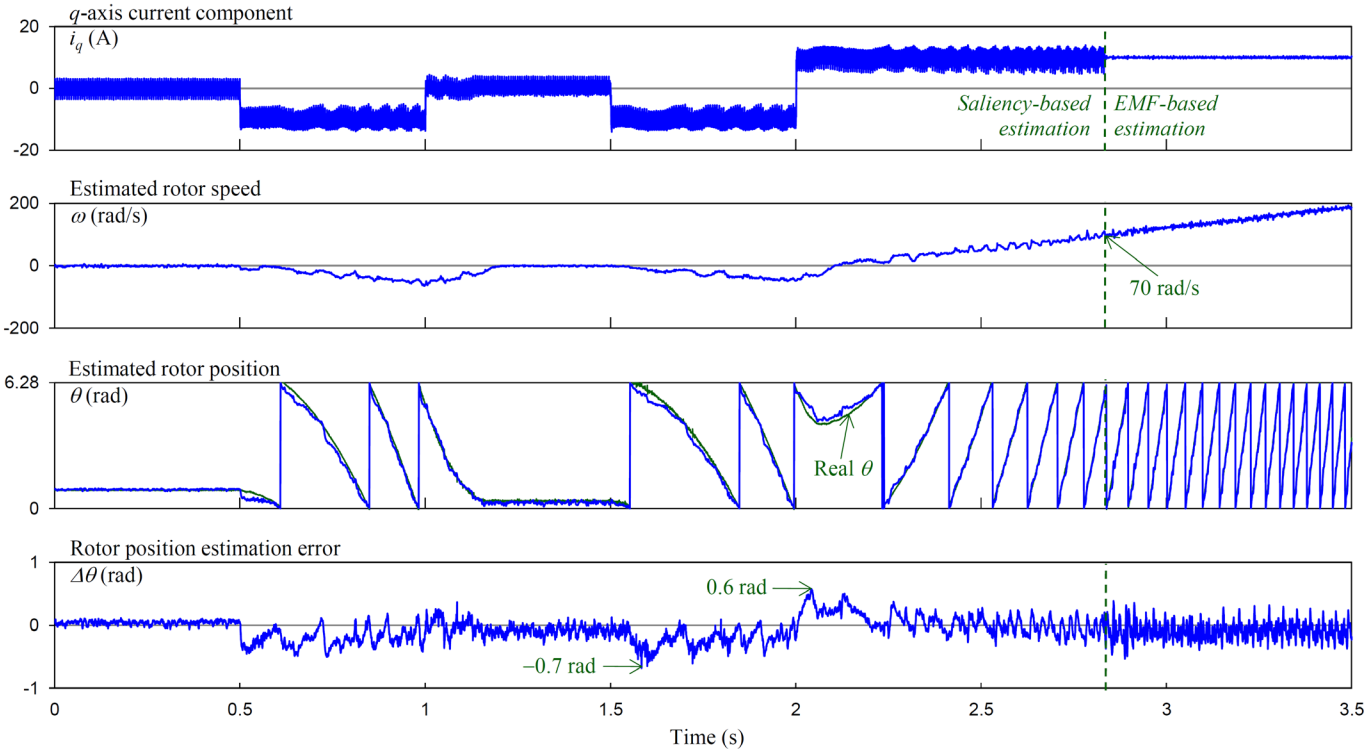


(b)

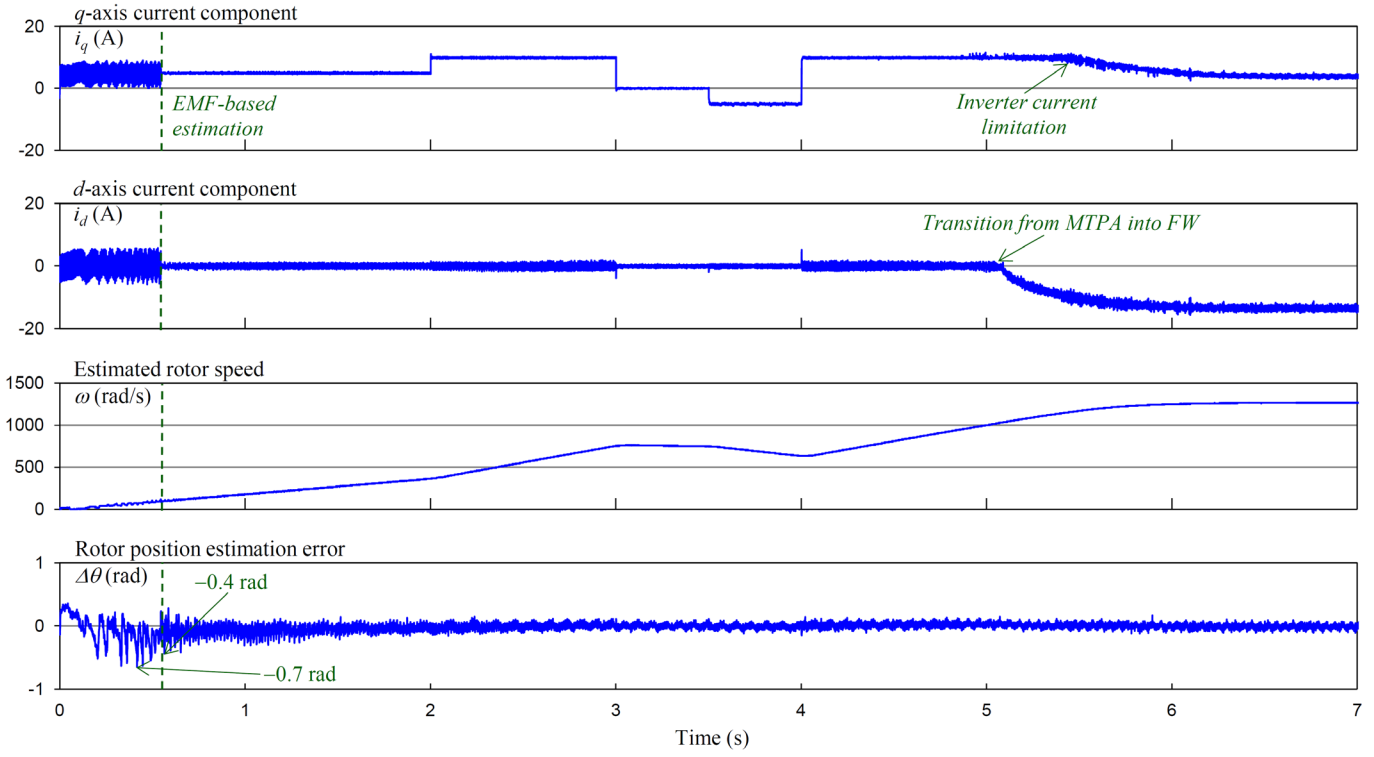

(c)

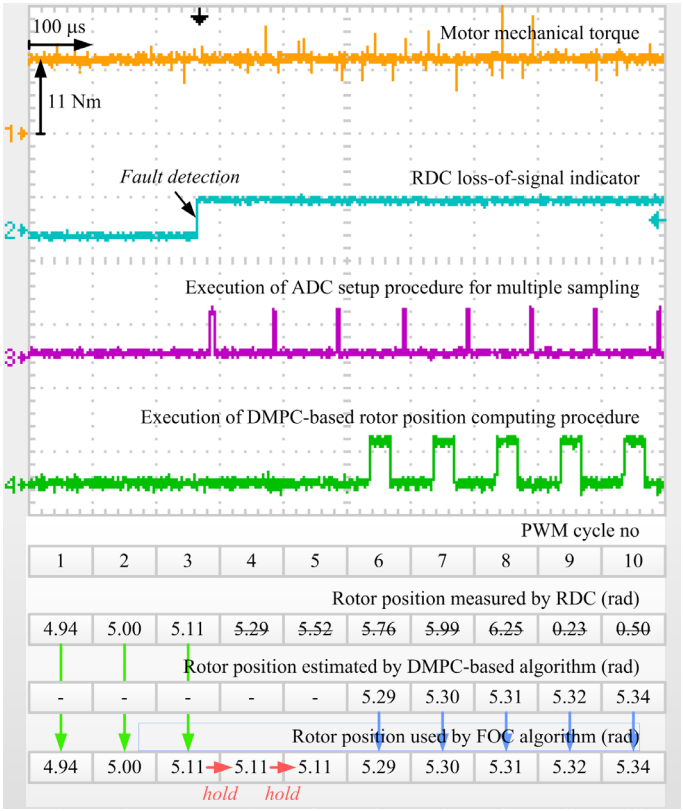


**Fig. 8.** Results of the experimental tests: (a) proof of full-torque feasibility at low speed; (b) proof of a stable operation at the full-speed range and different driving modes; (c) proof of stable drive behaviour upon the emergency start-up of the sensorless mode at $\omega = 650$ rad/s and $i_q = 5$ A

## 7. Conclusion

The paper's main contribution to vehicle emergency-backup control is an implementation of the DMPC estimators. The DMPC-based methods fulfil all the essential requirements for the fault-activated algorithms, on the contrary to the set of HF-injection and EMF-observer, which so far have been reported the only solution for flying-start applications. Although the proposed estimators show several drawbacks, such as drive power limitations and substantial current ripples occurring at low speeds, unacceptable in the most default applications of the sensorless algorithm, these disadvantages are not excludable in the emergency algorithms used only occasionally and temporarily.

The DMPC-based sensorless solution was tested under severe test scenarios. The results show that both tested rotor-position estimators proved their robustness under all assumed vehicle-specific operational conditions. The tests validated that the estimators implemented in an industrial-class controller enable the drive to switch into the sensorless mode upon a resolver fault and to operate stably without any hardware amendments.

The proposed implementation uses the indirect DMPC measurement, which requires a specific current-sampling approach, can be performed by a moderately sophisticated DSP without interrupting the main control loop. The estimation is based in the simple mathematical model comprising DMPCs; hence, the implementation of the proposed approach requires a low computational load. Moreover, since this load is applied only under the occurrence of a resolver fault, the processor's resources are available to manage the other possible faults.

The saliency-based estimator shows the greater estimation error than that of the EMF-based, most likely because of the low saliency of the motor used in this experiment. In vehicular applications, it would be typical to use IPMSMs of higher saliency and the error is expected to diminish. Other ways to improve the performance of the saliency-based estimator include increasing the duration of applying the test voltages, or increasing the resolution of the ADC converter, or using the sophisticated current sampling and processing algorithms such as proposed in [30]. However, since these methods affect the current ripples and implementation cost, a trade-off between them and the estimation error should be considered.

The simulated resolver failure results in a prompt response by the fault-detection algorithm implemented in hardware RDC. From this observation can be inferred that the last rotor's position determined by RDC before the loss-of-signal indication was accurate. Since not all faults may be detected promptly, the last RDC outcome sometimes may be incorrect; thus, the time to obtaining the first estimate is crucial to maintain vehicle stability. This motivates future work on shortening the DMPC measurement sequence required to compute the first estimate.

**References**


[1] P. J. King and K. J. Burnham, "Use of confidence limits in the setting of On-Board Diagnostic thresholds," in *Control (CONTROL), 2012 UKACC International Conference on*, 2012, pp. 708–712.

[2] B. Akin, S. Choi, and H. Toliyat, "DSP Applications in Electric and Hybrid Electric Vehicles [In the Spotlight]," *IEEE Signal Processing Magazine*, vol. 29, no. 3, pp. 136–133, May 2012.

[3] M. Bourogaoui, H. B. A. Sethom, and I. S. Belkhodja, "Real-time encoder faults detection and rotor position estimation for permanent magnet synchronous motor drives fault tolerant sensorless control using digital signal controller," *Mathematics and Computers in Simulation*.

[4] S. N. Foster, J. G. Cintron-Rivera, and E. G. Strangas, "Detection of incipient stator winding faults in PMSMs with single-layer fractional slot concentrated windings," *Electric Power Systems Research*, vol. 131, pp. 231–243, Feb. 2016.

[5] G. H. B. Foo, X. Zhang, and D. M. Vilathgamuwa, "A Sensor Fault Detection and Isolation Method in Interior Permanent-Magnet Synchronous Motor Drives Based on an Extended Kalman Filter," *IEEE Transactions on Industrial Electronics*, vol. 60, no. 8, pp. 3485–3495, Aug. 2013.

[6] Q.-X. Zhou, "Research on the signal process circuit and fault diagnosis of sine-cosine resolver," in *2011 International Conference on Electric Information and Control Engineering (ICEICE)*, 2011, pp. 5281–5284.

[7] M. Farina, E. Osto, A. Perizzato, L. Piroddi, and R. Scattolini, "Fault detection and isolation of bearings in a drive reducer of a hot steel rolling mill," *Control Engineering Practice*, vol. 39, pp. 35–44, Jun. 2015.
[8] K. Friedrischková, D. Vala, and B. Horák, "Testing of the traction batteries in electric vehicles and their further use," *IFAC-PapersOnLine*, vol. 48, no. 4, pp. 272–277, 2015.
[9] P. Nussbaumer, C. Macek, M. Ploechl, and T. M. Wolbank, "Dynamics of four-wheel-drive electric vehicle during machine fault condition," in *Power Electronics and Applications (EPE), 2013 15th European Conference on*, 2013, pp. 1–10.
[10] B. Li, H. Du, W. Li, and Y. Zhang, "Side-slip angle estimation based lateral dynamics control for omni-directional vehicles with optimal steering angle and traction/brake torque distribution," *Mechatronics*, vol. 30, pp. 348–362, Sep. 2015.
[11] W.-H. Kim, M.-J. Kim, K.-D. Lee, J.-J. Lee, J.-H. Han, T.-C. Jeong, S.-Y. Cho, and J. Lee, "NE-Map-Based Design of an IPMSM for Traction in an EV," *IEEE Transactions on Magnetics*, vol. 50, no. 1, pp. 1–4, Jan. 2014.
[12] A. El-Refaie, J. Alexander, K.-K. Huh, S. Galioto, P. Reddy, P. De Bock, and X. Shen, "Advanced High Power-Density Interior Permanent Magnet Motor for Traction Applications," *IEEE Transactions on Industry Applications*, pp. 1–1, 2014.
[13] I. Kim, H. Kim, T. Kwon, and H. Lee, "Fail-Safe Control Strategy of Traction Motor in Electric Mobility with Sensorless Control Scheme," in *Vehicular Technology Conference (VTC Spring), 2012 IEEE 75th*, 2012, pp. 1–5.
[14] M. Aguirre, J. Poza, L. Aldasoro, and T. Nieva, "Sensorless torque control of PMSMs for railway traction applications," in *2013 15th European Conference on Power Electronics and Applications (EPE)*, 2013, pp. 1–10.
[15] L. Jarzebowicz, "Sensorless IPMSM drive with rotor position estimator based on analysis of phase current derivatives," in *Industrial Electronics (ISIE), 2011 IEEE International Symposium on*, 2011, pp. 733–738.
[16] A. Accetta, M. Cirrincione, and M. Pucci, "TLS EXIN based neural sensorless control of a high dynamic PMSM," *Control Engineering Practice*, vol. 20, no. 7, pp. 725–732, Jul. 2012.
[17] K. Kondo, "PMSM and IM rotational sensorless technologies specialized for railway vehicles traction," in *2014 IEEE 5th International Symposium on Sensorless Control for Electrical Drives (SLED)*, 2014, pp. 1–7.
[18] S. M. Taghavi, M. Jain, and S. S. Williamson, "A comparative study of sensorless control techniques of interior permanent magnet synchronous motor drives for electric vehicles," in *2011 IEEE Vehicle Power and Propulsion Conference (VPPC)*, 2011, pp. 1–7.
[19] S. Bifaretti, V. Iacovone, A. Rocchi, P. Tomei, and C. M. Verrelli, "Nonlinear speed tracking control for sensorless PMSMs with unknown load torque: From theory to practice," *Control Engineering Practice*, vol. 20, no. 7, pp. 714–724, Jul. 2012.
[20] Y. Hua, M. Sumner, G. Asher, Q. Gao, and K. Saleh, "Improved sensorless control of a permanent magnet machine using fundamental pulse width modulation excitation," *IET Electric Power Applications*, vol. 5, no. 4, p. 359, 2011.
[21] S. Bolognani, S. Calligaro, R. Petrella, and M. Sterpellone, "Sensorless control for IPMSM using PWM excitation: Analytical developments and implementation issues," in *Sensorless Control for Electrical Drives (SLED), 2011 Symposium on*, 2011, pp. 64–73.
[22] P. Nussbaumer and T. M. Wolbank, "Using switching transients to exploit sensorless control information for electric machines," in *Sensorless Control for Electrical Drives (SLED), 2011 Symposium on*, 2011, pp. 35–40.

[23] D. Paulus, P. Landsmann, and R. Kennel, "Saliency based sensorless field-oriented control for permanent magnet synchronous machines in the whole speed range," in *Sensorless Control for Electrical Drives (SLED), 2012 IEEE Symposium on*, 2012, pp. 1–6.
[24] Ming-Yen Wei and Tian-Hua Liu, "A High-Performance Sensorless Position Control System of a Synchronous Reluctance Motor Using Dual Current-Slope Estimating Technique," *IEEE Transactions on Industrial Electronics*, vol. 59, no. 9, pp. 3411–3426, Sep. 2012.
[25] C.-K. Lin, L.-C. Fu, and T.-H. Liu, "A novel current-slope estimation strategy for sensorless position control of IPMSM without high-frequency signal injection," in *2011 SICE Annual Conference (SICE)*, Tokyo, 2011, pp. 2427–2432.
[26] Y. Hosogaya and H. Kubota, "Sensorless control method of IPMSM with Current derivative information of q-axis without High frequency component injection at Low speed region," in *Electrical Machines and Systems (ICEMS), 2012 15th International Conference on*, 2012, pp. 1–5.
[27] M. Schrodl and C. Simetzberger, "Sensorless control of PM synchronous motors using a predictive current controller with integrated INFORM and EMF evaluation," in *Power Electronics and Motion Control Conference, 2008. EPE-PEMC 2008. 13th*, 2008, pp. 2275–2282.
[28] Y. Hua, M. Sumner, G. Asher, and Q. Gao, "Sensorless Control for a PM Machine with Reduced Current Distortion using Space Vector PWM Excitation," in *13th European Conference on Power Electronics and Applications*, Piscataway, NJ, 2009.
[29] L. Jarzebowicz, "Indirect Measurement of Motor Current Derivatives in PMSM Sensorless Drives," *Elektronika ir Elektrotechnika*, vol. 20, no. 7, 2014.
[30] Y. Duan and M. Sumner, "A novel current derivative measurement using recursive least square algorithms for sensorless control of permanent magnet synchronous machine," in *Power Electronics and Motion Control Conference (IPEMC), 2012 7th International*, 2012, vol. 2, pp. 1193–1200.